2026 IEEE/SICE International Symposium on System Integration (SII)
January 11-14, 2026. Cancún, México

Development of a Compliant Mechanism for Series Elastic Actuators*

Amin Farjah[1], Jalal Taheri Kahnamouei[2], and Mehrdad Moallem[1]

Abstract— **This paper presents a comprehensive study on the design and performance of a rotational spring mechanism for Series Elastic Actuators (SEAs), fabricated using 3D printing techniques. The spring consists of six symmetrically arranged elastic blades that connect concentric inner and outer rings, enabling bidirectional compliance and large angular deflection. By systematically varying geometric parameters, particularly blade thickness, we investigate the influence on torque-displacement behavior and overall stiffness. A lumped parameter model is developed to analyze the spring mechanics under rotational deformation, and closed-form expressions for torque response are derived. An experimental setup is developed using a DC motor to apply torque to the designed springs and assess the torque-displacement relationship. The results provide key insights into how design parameters affect spring performance and offer practical guidelines for the development of lightweight, customizable compliant elements in next-generation robotic actuator systems.**

I. INTRODUCTION

Series Elastic Actuators (SEAs) are widely used in humanoid and compliant robots due to their ability to store and release energy, filter shocks, and enable precise force control [1] [2]. By integrating springs between the actuator and the load, Series Elastic Actuators have emerged as a prominent choice in robotic systems due to their capacity to enhance force controllability, mitigate impact forces, and improve operational safety [3] [4]. These devices provide a number of benefits over rigid actuators, including better torque control, energy storage capabilities [5] [6]. Building on these benefits, modern SEA designs increasingly incorporate innovative spring geometries and advanced materials to achieve compactness, durability, and high performance, which has expanded their application in wearable robotics [7], exoskeletons [8], prosthetics [9], and assistive devices [1].

Several recent works have also focused on SEA applications in wearable and assistive technologies. Al-Dahiree et al. [8] designed a compact energy storage mechanism using a rotary SEA for lumbar support exoskeletons, while Wang et al. [10] developed a series–parallel elastic actuator for weight-bearing exoskeletons, incorporating variable stiffness to adapt to different gait phases. In the domain of prosthetic devices, Carney and Herr [9] evaluated a reaction-force SEA configurable for biomimetic powered ankle and knee prostheses, emphasizing adaptability and energy efficiency. He et al. [11] recently proposed a compact SEA design compatible with MRI environments, highlighting the growing interest in precise, safe, and application-specific SEA modules. These developments illustrate the increasing need for compact, efficient, and tunable SEA components that can meet a wide variety of mechanical and functional demands.

A key factor in these advancements is the spring element, whose mechanical characteristics critically influence SEA performance. Key properties such as stiffness linearity, hysteresis, fatigue resistance, and energy density directly impact the torque control accuracy, bandwidth, and efficiency of the system [12] [13]. Studies have demonstrated that tailoring the spring's geometry, thickness, and material composition allows engineers to achieve desirable torque-displacement profiles for specific applications [14]. In particular, the integration of 3D printing technologies has enabled rapid prototyping and testing of custom springs with complex geometries [15] [16]. In recent years, innovative spring architectures and variable stiffness mechanisms have emerged as key enablers in advancing the functionality and versatility of SEAs. Yoon et al. [8] proposed a compact SEA for lumbar support exoskeletons featuring a spiral-shaped rotary spring optimized for high energy storage. Similarly, Mathew et al. [7] designed discoid elastic elements for humanoid robotic arms, focusing on achieving desirable stiffness profiles within compact volumes. Additionally, 3D-printed composite springs exhibiting high energy density were investigated by Han et al. [15], offering promising results for lightweight compliant robots. Beyond static stiffness, dynamic and variable stiffness mechanisms have been investigated to enhance SEA adaptability. Qian et al. [1] presented a reconfigurable SEA capable of switching between different stiffness profiles, improving versatility for assistive tasks. Shah and Saund [17] introduced a manipulator architecture based on passive variable stiffness, offering novel compliance solutions for legged robotic systems. Wang and Whitney [18] further demonstrated how a cable-driven rotary SEA could be optimized for upper limb rehabilitation, underscoring the importance of careful spring modeling in force control strategies.

Despite these advances, there remains a gap in systematic analytical studies that investigate how specific geometric parameters of springs—such as thickness variations—affect the mechanical response in rotary SEA applications. Most existing designs either rely heavily on finite element simulations or target specific use cases without offering generalized experimental insights into the relationship between geometry

*Research supported by the Natural Sciences and Engineering Research Council of Canada (NSERC) under the Discovery Grants program.

[1]Amin Farjah and Mehrdad Moallem are with the School of Mechatronic Systems Engineering, Simon Fraser University, Surrey, BC, Canada (Corresponding author e-mail: mmoallem@sfu.ca).

[2]Jalal Taheri Kahnamouei is with Mechanical Engineering Department, School of Energy, British Columbia Institute of Technology, Burnaby, BC, Canada

and stiffness characteristics, [19]. In addition, some of the existing spring designs are restricted to either clockwise or counterclockwise operation, or they produce noticeably different torque responses during compression versus decompression. This lack of symmetry can make them unsuitable for applications that require consistent and balanced bidirectional—a limitation that this study aims to overcome [20].

This work aims to address this gap by providing an analytic study to investigate a series of 3D-printed rotary springs with systematically varied thicknesses. We analyze how geometric modifications influence the resulting stiffness and torque-displacement profiles. The findings presented herein offer practical guidelines for the design of lightweight, customizable, and efficient springs tailored for SEAs in next-generation robotic applications.

II. MECHANICAL DESIGN OF THE ELASTIC ELEMENT

In this section, the design of the proposed elastic spring is discussed. The primary goals are to achieve bidirectional functionality with a symmetrical torque profile in both clockwise and counterclockwise directions. Additionally, the spring is intended to have a wide deflection working range while remaining compact, lightweight, and optimized for easy fabrication using 3D printing technology. The proposed elastic spring model contains three parts, adding bias elasticity to the mechanism as shown in Fig. 1. To study the proposed spring, a Linear Parameter Model (LPM) is used to determine an equivalent system representation, facilitating the simplification of the design, as shown in Fig. 2

The equivalent system consists of six springs created by the blades that symmetrically connect the inner and outer rings. These springs are arranged such that three are attached at angles γ_0, $120 + \gamma_0$, and $240 + \gamma_0$. The remaining three springs are positioned symmetrically in the opposite direction, connected at $-\gamma_0$, $-120-\gamma_0$, and $-240-\gamma_0$. The proposed spring configuration ensures a symmetric torque response in both clockwise and counterclockwise directions. This is achieved by arranging the blades so that, during rotation in either direction, three of the springs undergo compression while the other three are in tension. As a result, the equivalent stiffness remains nearly identical regardless of the direction of rotation, making the design well-suited for applications requiring bidirectional compliance. Additionally, the structural layout allows for a wide angular deflection range, supporting up to ±25 degrees (a total of 50 degrees), which is comparable to the capabilities reported in recent spring design studies [21].

Detailed derivations of spring elongations, updated angles, and corresponding torques are provided in the Appendix. The total restoring torque τ_t generated by the six springs is:

$$\tau_t = \sum_{i=1}^{6} \tau_i \tag{1}$$

Due to symmetry, this simplifies to:

$$\tau_t = 3\tau_{\text{tensile}} + 3\tau_{\text{compressed}} \tag{2}$$

where τ_t is the total restoring torque and the individual torque expressions (τ_{tensile} and $\tau_{\text{compressed}}$) are derived based on spring elongation and angle (see the Appendix). For small angular displacements, a linearized form of torque can be approximated using a Taylor expansion:

$$\tau_t \approx K_{eq}\theta \tag{3}$$

where K_{eq} is the effective rotational stiffness of the spring, derived in the Appendix, and can be expressed as:

$$K_{eq} = \frac{9}{2}\frac{R^2 r^2 K}{(R^2 + r^2 - Rr)} \tag{4}$$

where R is the radius of the outer ring, r is the radius of the inner ring, and K is the stiffness of the spring that is created by the inner blades as shown in Fig. 1.

Equation (4) illustrates that the equivalent stiffness is a function of the spring's stiffness as well as the radii of the inner and outer rings. Furthermore, the stiffness of each spring blade is influenced by its material characteristics and thickness. To investigate the effect of these parameters on the overall equivalent stiffness, a series of springs were fabricated using different materials and blade thicknesses.

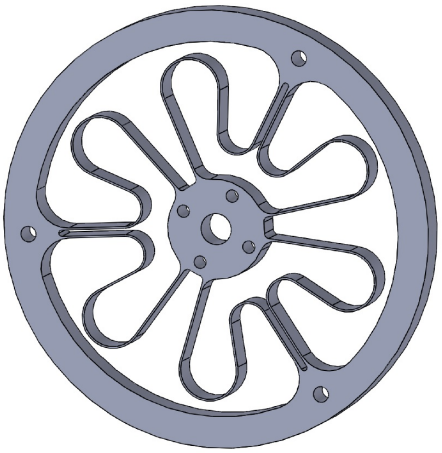

Fig. 1. Sketch model of elastic spring

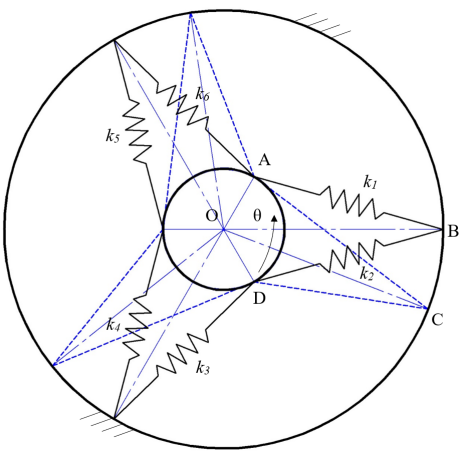

Fig. 2. Lumped parameter model of elastic spring

These springs were then evaluated through an experimental setup, which is explained in detail in the next section.

III. EXPERIMENTAL SETUP DESIGN AND SPRING MANUFACTURING

To investigate the influence of geometry on the stiffness characteristics of the designed rotary springs, a set of torsional springs was fabricated using 3D printing. Each spring is designed with identical outer ring (140 mm) and inner ring (32 mm) diameters, but varied in blade thickness to examine how cross-sectional geometry affects torque-deflection behavior. The material used for fabrication is nylon, chosen for its mechanical consistency and ease of manufacturing. The springs are designed and manufactured with three different blade thicknesses to examine how blade thickness influences the overall stiffness of the springs. These thicknesses are chosen to be 0.6 mm, 1.2 mm, and 2.4 mm, allowing for a comprehensive analysis of how varying material cross-sections affect the spring's stiffness and torque characteristics. The selected thicknesses were determined based on the minimum printable limit of the 3D printer, while the maximum thickness was restricted to 2.4 mm, as greater values would create an overly stiff structure that could not be tested with the available experimental setup. For each thickness, one set of springs was produced through 3D printing, as depicted in Fig. 3.

To measure the stiffness of these springs under rotational loading, a dedicated test-bench has been developed. This test bench includes a 250 W DC motor capable of delivering a continuous torque of up to 1.2 Nm. The motor includes an integrated quadrature encoder that is mounted directly on it to measure angular displacement. To estimate the motor's output torque, a Texas Instruments INA241A bidirectional in-line current sensor is employed. This sensor features advanced PWM rejection capabilities, enabling precise current measurements even in noisy environments. These current measurements are then used to estimate the motor torque through motor torque-current relationship. Additionally, the torque is estimated using the mechanical model of the machine to validate and cross-check the previous estimation. The torque estimates based on the instantaneous current measurement and the mechanical model are presented in equations (5) and (6), respectively, as follows:

$$\tau_{elec} = k_t i \tag{5}$$

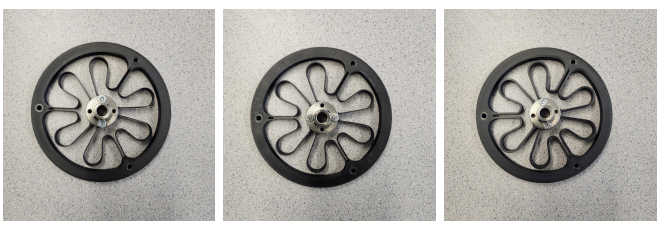

(a) (b) (c)

Fig. 3. 3D-printed springs with different blade thicknesses: (a) 0.6 mm, (b) 1.2 mm, and (c) 2.4 mm

$$\tau_{mech} = J \cdot \frac{d\omega}{dt} + B \cdot \omega \tag{6}$$

where τ_{elec} is the estimated torque through electrical model, τ_{mech} is the estimated torque through mechanical model, k_t is the motor's torque constant, i is the armature current, J is moment of inertia of the rotor, ω is the angular velocity, and B is viscous damping coefficient.

To control the operation of the motor, a dSPACE 1104 control unit is paired with BTS7960 dual H-bridge driver modules, allowing controlled bidirectional deflection of the spring. Finally, the spring's outer ring is bolted to the platform to hold it in place, while the inner ring is connected to the motor using a 10 mm rod, allowing the motor to apply torque to the spring. The experimental setup is shown in Fig. 4.

To further explore the impact of material properties on the equivalent stiffness, the Aluminum spring is designed with a 1.2 mm thickness, matching the size of the medium-sized 3D-printed spring for a direct comparison. The aluminum-made spring can be seen integrated within the experimental setup in Fig. 4. This setup is then used to measure the dynamic stiffness of the 3D-printed and Aluminum springs, whose results are presented in the next chapter.

IV. EXPERIMENTAL RESULTS

To assess the stiffness of the springs, the torque versus deflection relationship is determined using the developed setup. In the first test, the torque profile of the 0.6 mm, 1.2 mm, and 2.4 mm 3D-printed springs is compared when they are deflected -5 deg to +5 deg as depicted in Fig. 5. As shown in this figure, the 2.4 mm spring has an equivalent stiffness more than five times greater than that of the spring with 1.2 mm blades, whereas the 1.2 mm spring exhibits a stiffness approximately 50% higher than the spring with 0.6 mm blade thickness. The results demonstrate that the blade thickness has a polynomial relationship with the spring's stiffness, which means that higher stiffness levels can be achieved by simply increasing the blade thickness, without modifying the dimensions of the inner and outer rings. Furthermore, the spring exhibits a degree of hysteresis between compression and decompression phases, which is

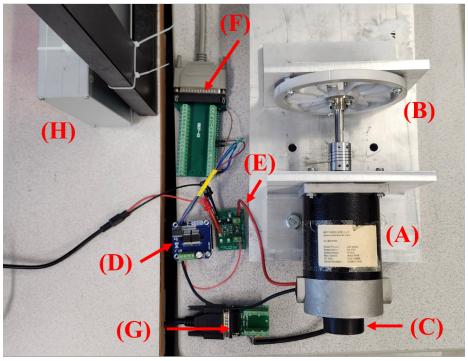

Fig. 4. Experimental setup including: (A) DC Motor, (B) designed spring, (C) quadrature encoder, (D) dual H-Bridge driver, (E) in-line current sensor, (F) signal interface board to dSPACE, (G) encoder interface board to dSPACE, and (H) dSPACE 1104 controller board.

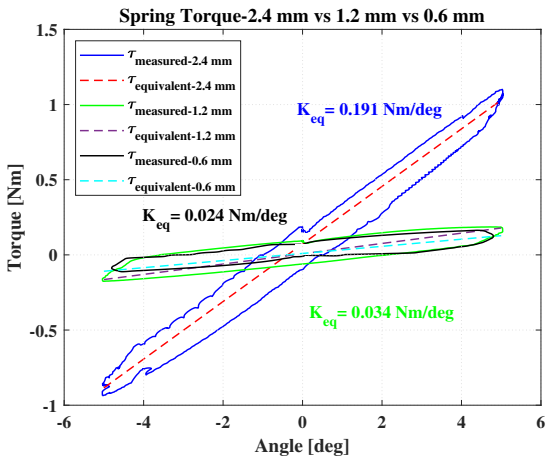

Fig. 5. The torque–angle relationship of the 3D-printed springs with 0.6 mm, 1.2 mm and 2.4 mm blade thickness

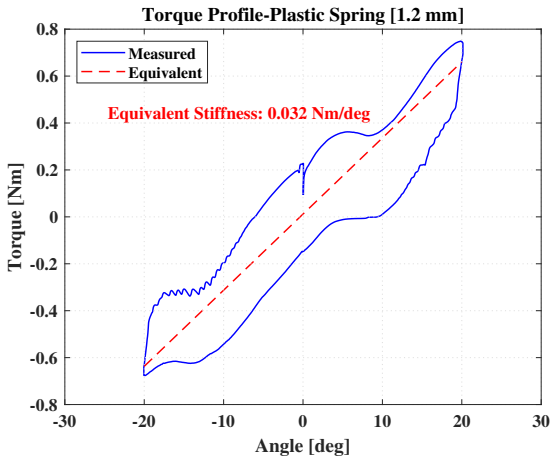

Fig. 7. The torque–angle relationship of the 3D-printed spring with a blade thickness of 1.2 mm, evaluated under a 20-degree angular deflection.

typical for torsional springs [22]. The width of the hysteresis band remains relatively consistent during operation, which is beneficial as it allows consistent operation of the spring during compression and decompression. Additionally, the calculated equivalent stiffness for each blade thickness can be compared with (4), which represents the effective rotational stiffness. Although all the springs share the same inner and outer ring diameters (r and R, respectively), variations in blade thickness lead to different stiffness values (K) for the blade springs.

The torque response of the 3D-printed spring with a 1.2 mm blade thickness is compared with an Aluminum counterpart that shares the same blade thickness and geometry. As shown in Fig. 6, the stiffness of the Aluminum spring is nearly ten times higher than that of the 3D-printed version, underscoring the significant influence of material properties on overall spring behavior. Springs with higher stiffness, such as the one made from Aluminum, are better suited for applications where precise control, minimal displacement, and fast dynamic response are required [22]. In contrast, the 3D-printed spring offers greater compliance, making it more appropriate for systems experiencing frequent vibrations or

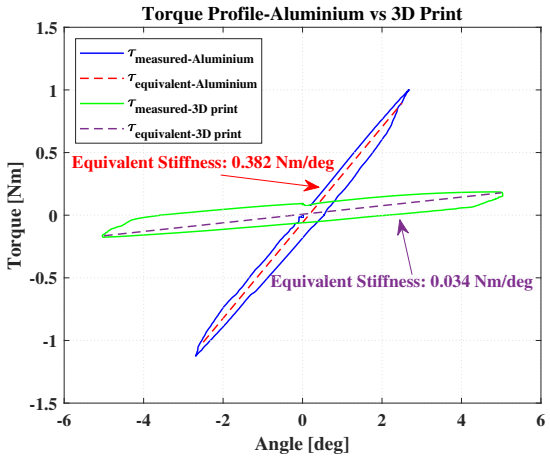

Fig. 6. The torque–angle relationship of Aluminum and 3D-printed springs with 1.2 mm blade thickness

requiring flexibility. Additionally, Fig. 6 reveals that the Aluminum spring exhibits a smaller hysteresis loop compared to the 3D-printed spring, which can be attributed to differences in how the materials behave during the compression and decompression cycles.

To evaluate the spring's behavior under larger angular deflections, the 1.2 mm blade spring was tested with a ±20-degree rotation, and its torque profile is presented in Fig. 7. The results indicate that the equivalent stiffness at this deflection (0.032 Nm/deg) is very close to the stiffness measured at ±5-degree deflection (0.034 Nm/deg), suggesting the spring maintains a relatively consistent stiffness over a wider range of motion. However, some degree of nonlinearity appears in the torque response, primarily due to the interaction of the six spring blades integrated into the design. Since the spring blades exhibit slightly different behaviors during compression and decompression, exceeding a certain deflection threshold causes the more heavily compressed blades to approach their mechanical limits, resulting in deviations from linearity. Nevertheless, such nonlinearities can be effectively compensated for by the actuator in a SEA system through appropriate torque control strategies [23].

Finally, the influence of blade thickness on the equivalent stiffness of 3D-printed springs is investigated by conducting a series of experiments on springs with varying blade thicknesses. The relationship between blade thickness and spring stiffness, based on test data from the 0.6 mm, 1.2 mm, and 2.4 mm 3D-printed springs, is depicted in Fig. 8. As shown in here, the stiffness increases in a polynomial manner with blade thickness, highlighting the strong dependence of mechanical performance on geometric parameters. Additionally, since hysteresis behavior was observed during testing, the plot is displayed as a band that spans the range between the minimum and maximum measured stiffness values for each blade thickness, better illustrating the variability and range of possible results.

Overall, the experiments demonstrate that the stiffness of the rotary spring is strongly affected by both the blade thickness and the material used. Springs with thicker blades

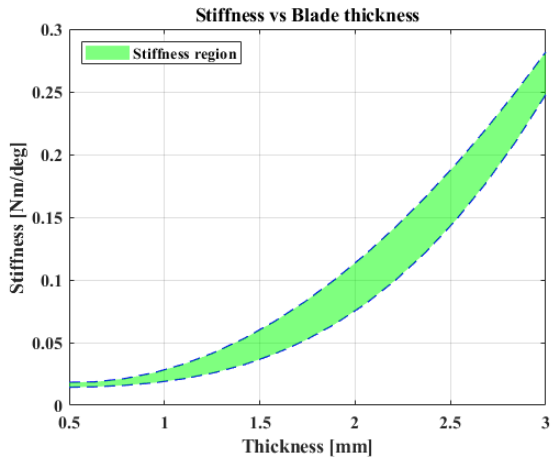

Fig. 8. Spring stiffness vs blade thickness of the 3D-printed springs.

or made from stiffer materials like Aluminum exhibit greater stiffness, whereas thinner, 3D-printed variants offer more flexibility. The spring maintains a relatively stable stiffness across different angular deflections, and while minor hysteresis and nonlinearity are present, they can be effectively handled with appropriate control methods.

V. CONCLUSIONS

This study presented the design, modeling, and preliminary analysis of a rotary spring-based elastic element intended for integration into a Series Elastic Actuator. The proposed design utilizes a 3D-printed rotary spring composed of multiple arc-shaped beams arranged symmetrically to provide a symmetric torque-displacement profile during both clockwise and counter-clockwise rotations. The mathematical model was developed using LPM to describe the spring's stiffness characteristics and was validated through experimental tests. The experimental results showed that the stiffness of the designed spring stiffness depends heavily on both blade thickness and material type. Springs made from stiffer materials or with thicker blades produce higher stiffness, while thinner, 3D-printed springs allow more flexibility. The spring also maintains consistent stiffness across various deflections, with minor hysteresis and nonlinearity that can be managed through control strategies when integrated in SEA configuration. The results confirm that the proposed design offers a lightweight, bidirectional spring that is easy to fabricate using standard 3D printers, while also allowing stiffness customization through changes in blade thickness to meet various application needs.

APPENDIX

The detailed derivations of governing equations of the designed spring are presented in this part In the pre-loaded configuration, the springs have an initial length l_0, defined as:

$$l_0 = \sqrt{R^2 + r^2 - 2Rr\cos 60^\circ} = \sqrt{R^2 + r^2 - Rr} \quad (7)$$

Using the law of sines, the initial angle γ_0 is:

$$\gamma_0 = \arcsin\left(\frac{r\sin 60^\circ}{l_0}\right) \quad (8)$$

When the outer ring rotates by angle θ, three springs stretch, each to a length l_i given by:

$$l_i = \sqrt{R^2 + r^2 - 2Rr\cos(60^\circ + \theta)} \quad i = 1, 3, 5 \quad (9)$$

The elongation Δl_i and γ_i of each stretched spring are:

$$\Delta l_i = l_i - l_0 \quad i = 1, 3, 5 \quad (10)$$

$$\gamma_i = \arcsin\left(\frac{r\sin(60^\circ + \theta)}{l_i}\right) \quad i = 1, 3, 5 \quad (11)$$

The rotation also compresses the remaining three springs, with their lengths l_j given by:

$$l_j = \sqrt{R^2 + r^2 - 2Rr\cos(60^\circ - \theta)} \quad j = 2, 4, 6 \quad (12)$$

The compression Δl_j and γ_j for each compressed spring are:

$$\Delta l_j = l_0 - l_j \quad j = 2, 4, 6 \quad (13)$$

$$\gamma_j = \arcsin\left(\frac{r\sin(60^\circ - \theta)}{l_j}\right) \quad j = 2, 4, 6 \quad (14)$$

The spring arrangement yields both compressive and tensile forces as the outer ring rotates, resisting its motion. The stretched and compressed springs generate torques τ_i and τ_j about the ring center, given by:

$$\tau_i = \Delta l_i kR\sin(\gamma_i) \quad (15)$$

$$\tau_j = \Delta l_j kR\sin(180^\circ - \gamma_j) = \Delta l_j kR\sin\gamma_j \quad (16)$$

Substituting equations (10) and (13) into (15) and (16), respectively, we obtain:

$$\tau_i = kRr\left[1 - \frac{\sqrt{R^2 + r^2 - Rr}}{\sqrt{R^2 + r^2 - 2Rr\cos(60^\circ + \theta)}}\right]\sin(60^\circ + \theta) \quad (17)$$

$$\tau_j = kRr\left[1 - \frac{\sqrt{R^2 + r^2 - Rr}}{\sqrt{R^2 + r^2 - 2Rr\cos(60^\circ - \theta)}}\right]\sin(60^\circ - \theta) \quad (18)$$

The total restoring torque τ_t, resulting from all six springs, simplifies due to their symmetrical arrangement to:

$$\tau_t = \sum_{p=1}^{3} \tau_p + \tau_{p+1} \quad (19)$$

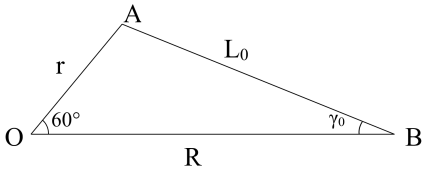

Fig. 9. Spring in the equilibrium position

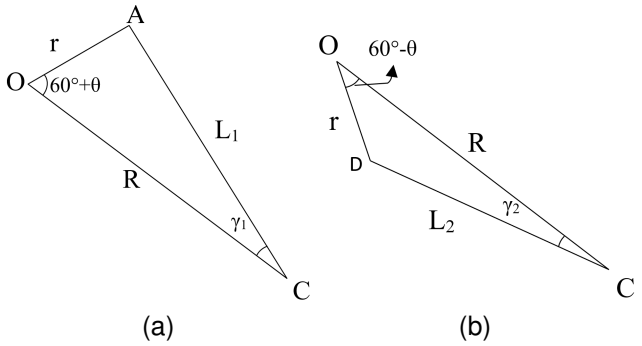

Fig. 10. Spring deformation after a clockwise rotation by an angle θ: (a) Spring 1 under tensile force, and (b) Spring 2 under compression force

Given that the stretched springs produce equal torque ($\tau_1 = \tau_3 = \tau_5$) and the compressed springs also exert equal torque ($\tau_2 = \tau_4 = \tau_6$), the total restoring torque τ_t is :

$$\tau_t = 3kRr\left[1 - \frac{\sqrt{R^2 + r^2 - Rr}}{\sqrt{R^2 + r^2 - 2Rr\cos(60^\circ + \theta)}}\right]\sin(60^\circ + \theta) + 3kRr\left[1 - \frac{\sqrt{R^2 + r^2 - Rr}}{\sqrt{R^2 + r^2 - 2Rr\cos(60^\circ - \theta)}}\right]\sin(60^\circ - \theta) \tag{20}$$

Using a Taylor series expansion and considering the first two terms, the total torque τ_t as a function of θ is approximated as:

$$\tau_t = f(\theta) \implies \tau_t \approx f(0) + \left(\frac{\partial f}{\partial \theta}\right)_{\theta=0}\theta \tag{21}$$

Since the springs are at rest when $\theta = 0$, the first term, $f(0)$, is zero. For the second term in the expansion, we have:

$$\frac{\partial f}{\partial \theta} = \frac{3R^2r^2K(R^2 + r^2 - Rr)}{\sqrt{[R^2 + r^2 - 2Rr\cos(60^\circ + \theta)]^3}}\sin^2(60^\circ + \theta) + \frac{3R^2r^2K(R^2 + r^2 - Rr)}{\sqrt{[R^2 + r^2 - 2Rr\cos(60^\circ - \theta)]^3}}\sin^2(60^\circ - \theta) \tag{22}$$

By setting $\theta = 0$ and substituting it into (3), we obtain:

$$\tau_t = \frac{9}{2}\frac{R^2r^2K}{(R^2 + r^2 - Rr)} \times \theta \tag{23}$$

Thus, the equivalent stiffness K_{eq} of the entire system is:

$$K_{eq} = \frac{9}{2}\frac{R^2r^2K}{(R^2 + r^2 - Rr)} \tag{24}$$

ACKNOWLEDGMENT

This research was supported by the Natural Sciences and Engineering Research Council of Canada (NSERC) under the Discovery Grants program.

REFERENCES

[1] Y. Qian, S. Han, G. Aguirre-Ollinger, C. Fu, and H. Yu, "Design, modeling, and control of a reconfigurable rotary series elastic actuator with nonlinear stiffness for assistive robots," *Mechatronics*, vol. 86, p. 102872, 2022.

[2] M. K. Sharma, "A new variable stiffness series elastic actuator for the next generation collaborative robot," PhD Thesis, University of Dayton, Electrical and Computer Engineering, 2020.

[3] M. Donald and Q. Li, "Design and performance evaluation of a rotary series elastic actuator," in *Intelligent Robotics and Applications*. Springer Berlin Heidelberg, 2012, pp. 555–564.

[4] J. Hurst and K. Green, "Series elastic actuation," *Encyclopedia of Robotics, Springer Berlin Heidelberg*, pp. 1–12, 2020.

[5] M. C. Yildirim, A. T. Kansizoglu, P. Sendur, and B. Ugurlu, "High power series elastic actuator development for torque-controlled exoskeletons," in *4th International Symposium on Wearable Robotics*. Springer International Publishing, 2019, pp. 70–74.

[6] K. Kong, J. Bae, and M. Tomizuka, "Control of rotary series elastic actuator for ideal force-mode actuation in human–robot interaction applications," *IEEE/ASME Transactions on Mechatronics*, vol. 14, no. 1, pp. 105–118, 2009.

[7] X. Huo, Y. Xia, Y. Liu, L. Jiang, and H. Liu, "Design and development of a rotary serial elastic actuator for humanoid arms," in *Intelligent Robotics and Applications*. Springer International Publishing, 2014, pp. 266–277.

[8] O. S. Al-Dahiree, R. A. Raja Ghazilla, H. J. Yap, M. Osman Tokhi, and G. W. Yoong, "Modeling and dynamic performance of energy storage -rotary series elastic actuator for lumbar support exoskeleton," in *2022 IEEE 10th Conference on Systems, Process & Control (ICSPC)*, 2022, pp. 208–216.

[9] M. Carney, "Design and evaluation of a reaction-force series elastic actuator configurable as biomimetic powered ankle and knee prostheses," PhD Thesis, Massachusetts Institute of Technology, 2020.

[10] T. Wang, T. Zheng, S. Zhao, D. Sui, J. Zhao, and Y. Zhu, "Design and control of a series–parallel elastic actuator for a weight-bearing exoskeleton robot," *Sensors*, vol. 22, no. 3, p. 1055, 2022.

[11] B. He, N. Zhao, D. Y. Guo, C. H. Paxson, A. D. Goyeneche, M. Lustig, C. Liu, and R. S. Fearing, "Design and control of a compact series elastic actuator module for robots in mri scanners," *Robotics*, p. arXiv:2406.07670, 2025.

[12] G. Tonietti, R. Schiavi, and A. Bicchi, "Design and control of a variable stiffness actuator for safe and fast physical human/robot interaction," in *Proceedings of the 2005 IEEE International Conference on Robotics and Automation*, 2005, pp. 526–531.

[13] A. Farjah and M. Moallem, "Realization of efficient rotational springs and series elastic actuators using DC motors," in *2024 IEEE 18th International Conference on Control & Automation (ICCA)*, 2024, pp. 522–527.

[14] O. S. Al-Dahiree, R. A. R. Ghazilla, M. O. Tokhi, H. J. Yap, and M. Gul, "Design and characterization of a low-cost and efficient torsional spring for ES-RSEA," *Sensors*, vol. 23, no. 7, p. 3705, 2023.

[15] A. Sutrisno and D. J. Braun, "High-energy-density 3d-printed composite springs for lightweight and energy-efficient compliant robots," *Robotics*, p. arXiv:2211.09245, 2022.

[16] F. Hu, W. Wang, J. Cheng, and Y. Bao, "Origami spring-inspired metamaterials and robots: An attempt at fully programmable robotics," *Sci. Prog.*, vol. 103, no. 3, 2020.

[17] S. Shah and B. Saund, "SiMPLeR: A series-elastic manipulator with passive variable stiffness for legged robots," in *2021 6th International Conference on Automation, Control and Robotics Engineering (CACRE)*, 2021, pp. 73–80.

[18] C. Wang and J. P. Whitney, "Series Elastic Force Control for Soft Robotic Fluid Actuators," *Robotics*, p. arXiv:2004.01269, 2020.

[19] G. Lin, X. Zhao, J. Han, and Y. Zhao, "The optimum design of torsional spring for series elastic actuator," in *2017 IEEE 7th Annual International Conference on CYBER Technology in Automation, Control, and Intelligent Systems (CYBER)*, 2017.

[20] C. Irmscher, E. Woschke, E. May, and C. Daniel, "Design, optimisation and testing of a compact, inexpensive elastic element for series elastic actuators," *Medical Engineering & Physics*, vol. 52, pp. 84–89, 2018.

[21] B. Sheng, X. Lei, S. Q. Xie, and C. Wang, "Design and evaluation of a series elastic actuator based on parallel springs," in *2024 30th International Conference on Mechatronics and Machine Vision in Practice (M2VIP)*, 2024, pp. 1–5.

[22] Z. Bons, G. C. Thomas, L. Mooney, and E. J. Rouse, "An energy-dense two-part torsion spring architecture and design tool," *IEEE/ASME Transactions on Mechatronics*, vol. 29, no. 3, pp. 2373–2384, 2024.

[23] W. Wang and S. Sugano, "Output torque regulation through series elastic actuation with torsion spring hysteresis," in *2014 IEEE International Conference on Robotics and Biomimetics (ROBIO 2014)*, 2014, pp. 701–706.